Tidal Tomography Reveals a Thermal Anomaly Beneath Mars's Crustal Dichotomy

Alexander Berne[1*], Nicholas Wagner[2], Isamu Matsuyama[1], Sander Goossens[3], Antonio Genova[4], Marc Rovira-Navarro[5], Amirhossein Bagheri[6], Chuan Qin[7], Angela Marusiak[1], Douglas Hemingway[8], Harriet Lau[2], Kar Wai Cheng[9], Shijie Zhong[10], Francis Nimmo[11]

[1*]Lunar and Planetary Laboratory, University of Arizona, Tucson, AZ, 85721, USA.
[2]Department of Earth, Environmental and Planetary Sciences, Brown University, Providence, RI, 02912, USA.
[3]Planetary Geology, Geophysics, and Geochemistry Laboratory, NASA Goddard Space Flight Center, Greenbelt, MD, 20771, USA.
[4]Department of Mechanical and Aerospace Engineering, Sapienza University of Rome, Rome, Italy.
[5]Department of Geoscience and Engineering, Delft University of Technology, Delft, The Netherlands.
[6]Division of Geological and Planetary Sciences, California Institute of Technology, Pasadena, CA, 91125, USA.
[7]Department of Earth, Planetary, and Space Sciences, University of California, Los Angeles (UCLA), Los Angeles, CA, 90095, USA.
[8]Institute for Geophysics, Jackson School of Geosciences, University of Texas at Austin, Austin, TX, 78729, USA.
[9]Institute of Earth Sciences, Academia Sinica, Taipei, Taiwan.
[10]Department of Physics, University of Colorado Boulder, Boulder, CO, 80309, USA.
[11]Department of Earth and Planetary Sciences, University of California, Santa Cruz, Santa Cruz, CA, 95064, USA.

*Corresponding author(s). E-mail(s): aberne@arizona.edu;

Abstract

Mars undergoes seasonal tidal forcing due to its eccentric orbit and the tilt of its rotation axis relative to the Sun[1]. Response to this forcing produces temporal variations in the Martian gravity field and is sensitive to the planet's internal structure[2–4]. Using tracking data from the Mars Global Surveyor, Mars Odyssey, and Mars Reconnaissance Orbiter spacecraft[5–7], we demonstrate that degree-3 components of Mars's time-variable gravity field differ by up to 300% from predictions for a spherically symmetric planet[8–10]. These deviations can be explained if the effective shear modulus of the mantle varies by >20% over a roughly North-South pattern that closely aligns with the surface expression of the Martian crustal dichotomy[11]. Based on this correlation, we infer preservation of a 200–400°C thermal anomaly in the present-day mantle below Mars's Southern highlands. This temperature variation could reflect regional mantle convection[12;13] or insulation by Mars's thick Southern Highlands crust that has persisted over several billion years[14;15].

Keywords: Mars, tides, gravity, geodesy, dichotomy, mantle structure

Mars exhibits a prominent dichotomy in crustal structure. Whereas low-lying plains cover Mars' Northern hemisphere, the Southern hemisphere is more topographically elevated, rugged, and densely cratered[16]. These asymmetries potentially accompany an approximately 25 km mean variation in crustal thickness[11] (or a ∼200 kg m^{-3} variation in crustal density[17;18]) as well as spatial differences in crustal magnetization[19] and seismic wave attenuation[20]. The Northern lowlands may also have held surface water prior to the loss of Mars's putative oceans to space[21]. Understanding the origin of Mars's crustal dichotomy therefore constrains the planet's ancient hydrology and the timing of surface conditions capable of supporting life[22].

The origin of Mars's hemispheric crustal dichotomy is widely debated. Some studies suggest that a giant impact disrupted the planet's primordial mantle and either thickened the crust across the Southern hemisphere[23;24] or excavated the Northern hemisphere[25]. Other studies suggest that mantle convection over one hemisphere drives subsidence and resurfacing of the Northern crust or thickening and uplift of the Southern crust[12;13]. These formation hypotheses for the crustal dichotomy predict long-lived structures within the Martian deep interior that may persist into the present-day[12;13;23;24]. For example, crustal thickening over the Southern hemisphere could enhance thermal insulation and radiogenic heating of the deeper interior, resulting in a structurally weak underlying mantle[14;15]. Here, we investigate the character of these potential heterogeneities at depth by analyzing Mars's gravitational response to seasonal (that is, 687 Earth day) tidal interactions with the Sun.

The Martian gravity field can be expressed in terms of spherical harmonic coefficients of degree ℓ and order m ($C_{\ell m}$ and $S_{\ell m}$), with the full wavelength at a given ℓ usually defined as roughly $2\pi R/\ell$ ($R = 3,396$ km)[26]. Temporal variations can be modeled as cyclic perturbations to these coefficients and separated into in-phase (or 'cosine', A) and (a quarter cycle) out-of-phase (or 'sine', B) components over a given period (that is, $\Delta C_{\ell m}^{A,B}$ and $\Delta S_{\ell m}^{A,B}$) (see Methods). For a spherically symmetric planet, forcing at a given degree and order excites deformation only at the same degree and order. In this case, tidal forcing acts almost entirely at degree-2 and will contribute negligibly to Mars's gravity field at higher degrees (that is, $\Delta C_{3m}^{A,B}$, $\Delta S_{3m}^{A,B} \approx 0$). However, lateral heterogeneity in Mars's internal structure (for example, North-South variations in shear modulus) can couple with degree-2 forcing to produce substantial degree-3 signals such that $\Delta C_{3m}^{A,B}, \Delta S_{3m}^{A,B} \neq 0$[8]. Moreover, although static gravity fields carry some sensitivity to deep-seated density structure (especially at long wavelengths), their sensitivity is weighted toward structure in the shallower interior at all degrees (Eq. 4 of[27]). By contrast, Mars's low-order non-zonal (that is,

$m \neq 0$) time-variable gravity field is most sensitive to lateral variations in the shear modulus of the mantle since these heterogeneities generate larger mass redistributions than comparable perturbations within shallower layers[4;9]. Measuring time-variable gravity signals (for example, by analyzing the trajectory of orbiting spacecraft) correspondingly provides a direct means to constrain the extent of Mars's deep-seated heterogeneities[4].

Measuring Mars's Seasonal Tidal Response

To recover Mars's seasonal degree-3 tidal signals, we analyze Earth-based X-band Doppler tracking data acquired by the Deep Space Network (DSN) from multiple Martian orbiters. We use radio science data from Mars Global Surveyor (MGS), Mars Odyssey (ODY), and Mars Reconnaissance Orbiter (MRO) spanning a total of 16 years. Our data processing procedure follows the approach used to determine Mars's time-varying zonal ($m = 0$) gravity field in[28], but is extended in this study to include non-zonal $\ell = 2$ and $\ell = 3$ time-varying gravity field coefficients over the seasonal (or annual) 687-day period.

Recovered non-zonal degree-3 gravity field coefficient perturbations are presented in Table 1 (for zonal and degree-2 coefficients, see Extended Data Table 1). To account for modeling uncertainties, particularly those arising from unmodeled non-gravitational accelerations, we inflate the formal uncertainties of these coefficients by a factor of 15 (see, for example,[4]) in Table 1 and in all subsequent analysis. As in[28], we directly model the effects of the atmosphere by integrating the impact of the Mars General Circulation Model (GCM) on gravity coefficients (see Methods and Extended Data Figs. 1 and 2).

Table 1 Recovered degree-3 non-zonal time-varying gravity field for Mars with 15x formal uncertainties. Coefficient amplitudes are 4π-normalized and evaluated over the seasonal, 687-day period referenced to the J2000 epoch. Superscripts A and B denote in-phase (cosine) and out-of-phase (sine) signal components. Presented values correspond with the solid-body response (that is, blue bars) shown in Fig. 1a. Reported 15x formal 1-σ bounds are larger than (and therefore implicitly account for) uncertainties associated with inter-year variations in the Martian gravity field from our nominal atmospheric model (Fig. 1a), but do not directly consider the impact of extreme atmospheric models on coefficients (e.g., very warm, cold, or high dust conditions, see Methods and Extended Data Fig. 1).

Parameter	Amplitude	15x formal 1-σ Uncertainty
ΔC_{31}^{A}	-2.5084×10^{-10}	4.86×10^{-11}
ΔC_{31}^{B}	6.2830×10^{-12}	4.65×10^{-11}
ΔC_{32}^{A}	-2.7967×10^{-11}	3.17×10^{-11}
ΔC_{32}^{B}	7.9724×10^{-11}	3.44×10^{-11}
ΔC_{33}^{A}	1.0453×10^{-11}	3.95×10^{-11}
ΔC_{33}^{B}	1.6420×10^{-12}	4.07×10^{-11}
ΔS_{31}^{A}	-8.5201×10^{-11}	4.91×10^{-11}
ΔS_{31}^{B}	1.3759×10^{-10}	4.62×10^{-11}
ΔS_{32}^{A}	5.2115×10^{-11}	3.12×10^{-11}
ΔS_{32}^{B}	-1.3930×10^{-11}	3.41×10^{-11}
ΔS_{33}^{A}	9.1466×10^{-11}	3.95×10^{-11}
ΔS_{33}^{B}	1.0699×10^{-10}	4.07×10^{-11}

Modeling Mars's Mantle Structure

We recover non-zonal $\ell = 3$ perturbations to the Martian gravity field that deviate substantially from values predicted for a spherically symmetric Mars with an atmosphere (Fig. 1a). For example, the cosine coefficient of the $\ell = 3$, $m = 1$ gravity field perturbation (that is, ΔC_{31}^{A}) deviates approximately 300% from expectations for a spherically symmetric Mars with atmospheric loading (with >99.99% confidence, the difference between green and red bars in Fig. 1a), suggesting coupling between tidal deformation and laterally heterogeneous internal structure in Mars's mantle (Fig. 1b). To constrain the nature of these asymmetries, we perform a Bayesian, Markov chain Monte Carlo (MCMC) inversion (Methods). Inversions incorporate both Mars's degree-2 and degree-3 (zonal and non-zonal) time-variable gravity field as constraints (see Table 1, Extended Data Table 1, and Methods).

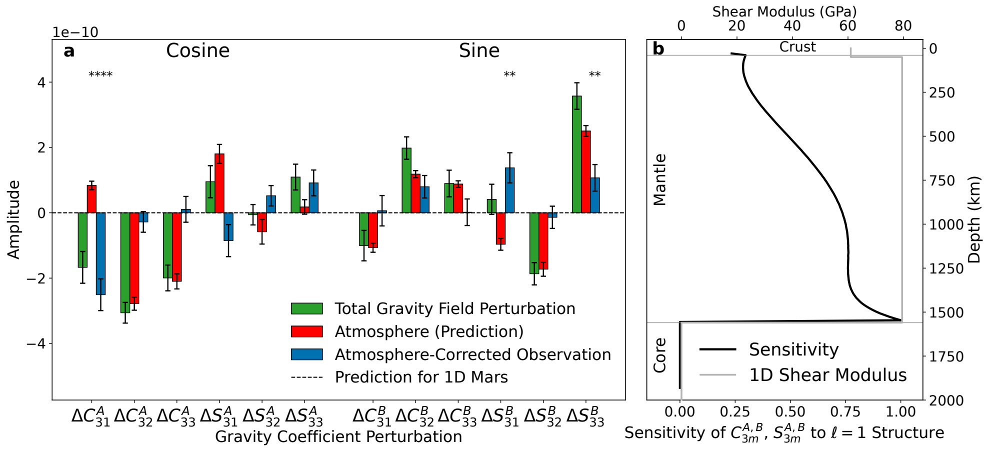

Fig. 1 Sensitivity of the Martian seasonal gravity field to laterally heterogeneous structure. **(a)** Bar chart showing the amplitude of seasonal temporal variations in selected Martian $\ell = 3$ gravity field coefficients (i.e., $\Delta C^{A,B}_{3m}$ and $\Delta S^{A,B}_{3m}$ where A and B denote cosine and sine terms). Green, red, and blue bars respectively denote the total gravity field perturbations, the predicted impact of the atmosphere on perturbations, and the observed gravity field perturbations corrected for the atmosphere. Error bounds on the green and blue bars represent 15× formal 1-σ uncertainties and stars denote statistical significance of the atmosphere corrected observation relative to the null hypothesis (that is, expectations for a spherically symmetric Mars with no atmosphere; Amplitude = 0, the horizontal dotted line). ** indicates a p-value of $p < 0.01$ and **** indicates $p < 0.0001$ for two-tailed t-tests. Error bars on predictions for red bars are 1-σ uncertainties computed by comparing inter-annual variations in the assumed atmospheric model (see Extended Data Fig. 1). Error bars on atmosphere-corrected coefficients (blue bars) are generally much larger than (and therefore implicitly account for) uncertainties associated with inter-year variations in the Martian gravity field from our nominal atmospheric model (red bars), but do not directly consider the impact of extreme atmospheric models on coefficients (see Methods and Extended Data Fig. 1). **(b)** Normalized sensitivity of gravity coefficients to ℓ=1 perturbations in shear modulus versus depth for Martian interiors subject to $\ell = 2$ tidal forcing. The average shear modulus with depth assumed for Mars is plotted as a gray line for reference (see Extended Data Table 2). Labels refer to vertical regions spanning the crust (0–50 km depth), the mantle (50–1,560 km) and the core (1,560–3,390 km).

Our model space consists of lateral shear modulus variations imposed onto a one-dimensional (1D) reference interior constrained by Mars's degree-2 tidal Love number, moment of inertia, and seismic travel-time data (see Extended Data Table 2,[29]). We expand these variations in a spherical harmonic basis truncated at degree $\ell = 3$ across two internal layers: the crust (0–50 km depth) and the mantle (50–1,560 km depth). Lateral crustal thickness and density variations on Mars negligibly ($< 0.3\%$) impact the time-variable gravity field and are therefore ignored for inversions. Heterogeneities in the core (including a potential solid inner layer[30]) also minimally affect time-variable gravity fields (Fig. 1b). We consequently prescribe a uniform elastic structure below 1,560 km depth. We use the semi-analytical spectral code LOV3D[10] to forward compute coupling between degree-2 forcing and lateral heterogeneity for candidate interior structures (see Methods). Note that Mars's zonal gravity field variations are additionally sensitive to seasonal CO_2 condensation over the polar caps[31]. We accordingly model $m = 0$ terms as the sum of the solid-body tide and a seasonal mass exchange of 6.2×10^{15} kg and 8.4×10^{15} kg over the northern and southern polar caps, respectively[28] (see Methods).

Our results indicate that degree-1 ($\ell = 1$) shear modulus structure, which reflects a hemispheric pattern, enhances the amplitude of $\ell = 3$ coefficients for Martian interiors subject to seasonal tidal forcing at $\ell = 2$ (Fig. 1b). For example, the $\ell = 2$, $m = 1$ harmonic associated with Mars's obliquity tide interacts with North-South (that is, $\ell = 1$, m = 0) shear modulus structure (lower/higher shear modulus values in the mid-latitudes of the Southern/Northern portions of the meridional hemisphere that spans -90°E to 90°E longitude) to regionally increase/decrease outward radial deformation. The resulting mass displacement yields an $\ell = 3$, $m = 1$ gravity signature that enhances the amplitude of ΔC_{31}^{A}. Interaction between other hemispherical variations such as East–West ($\ell = 1$, m = -1) and meridional ($\ell = 1$, m = 1) asymmetries and the full degree-2 Martian tide (that is, components arising from both Mars's obliquity and eccentricity) is more complex[10] but produces deviation of several degree-3 gravity coefficients from zero (see Extended Data Fig. 3). In contrast, the degree-2 time-variable gravity field does not measurably deviate from predictions for a spherically symmetric interior (Extended Data Fig. 3), suggesting minimal internal heterogeneity that strongly couples with $\ell = 2$ forcing (e.g., $\ell = 2$ patterns, see Extended Data Fig. 4)[10].

Our inversions predict statistically significant degree-1 variations in the Martian mantle's shear modulus. Specifically, we resolve North–South, meridional, and East–West patterns with peak-to-peak amplitudes (and 3-σ uncertainties) of $60 \pm 40\%$, $42 \pm 38\%$, and $36 \pm 34\%$ respectively (Fig. 2a–c) as well as an overall variation of $81 \pm 60\%$ (or >20%). Inversions fit all time-variable gravity field constraints to within 3-σ uncertainty (see Extended Data Fig. 3) and do not recover any statistically significant lateral variations in shear modulus for Mars's crust (Extended Data Table 3 and Extended Data Fig. 4a) or for degrees higher than $\ell = 1$ in the mantle (Extended Data Table 3 and Extended Data Fig. 4b). Note that heterogeneity amplitudes represent averages over the entire mantle depth range. This averaging is necessary to produce statistically significant results since the sensitivity of degree-3 time-variable gravity to 3D structure varies somewhat gradually with depth (Fig. 1b), resulting in substantial non-uniqueness between recovered heterogeneity amplitudes when the mantle is subdivided into multiple layers (see Extended Data Fig. 5). Even so, our inversions do not necessarily preclude more vertically localized structure within Mars's mantle (for example, at the base of the lithosphere[14] or near the core-mantle boundary[32]).

Mars's hemispheric mantle shear modulus variation broadly matches the spatial pattern of the crustal dichotomy (see Fig. 2d). For example, combining maximum likelihood solutions for recovered degree-1 order-1,0,-1 variations (see Fig. 2a–c) results in a region of elevated shear modulus beneath the Northern lowlands (centered at 45°N 138°W over Vastitas Borealis, see Fig. 2d) and a corresponding reduction in shear modulus beneath the Southern highlands (centered at 45°S 42°E near Hellas basin, see Fig. 2d). The zero-value contour of Mars's mantle shear modulus variation also tracks the boundary of the crustal dichotomy, including its Southward (or Northward) deflection over the anti-meridional (or meridional) hemisphere. The correspondence between surface geology and mantle stiffness variations weakens between 40°W and 139°W near the volcanic Tharsis rise region, potentially due to overprinting of the dichotomy boundary by this structure[33]. The lack of anomalies observed directly beneath Tharsis (Fig. 2d) also suggests that present-day internal structures associated with this feature are either small in amplitude (that is, compared to asymmetries in Fig. 2), shallow, or restricted to a relatively small ($\ell > 3$) lateral region within the interior[34].

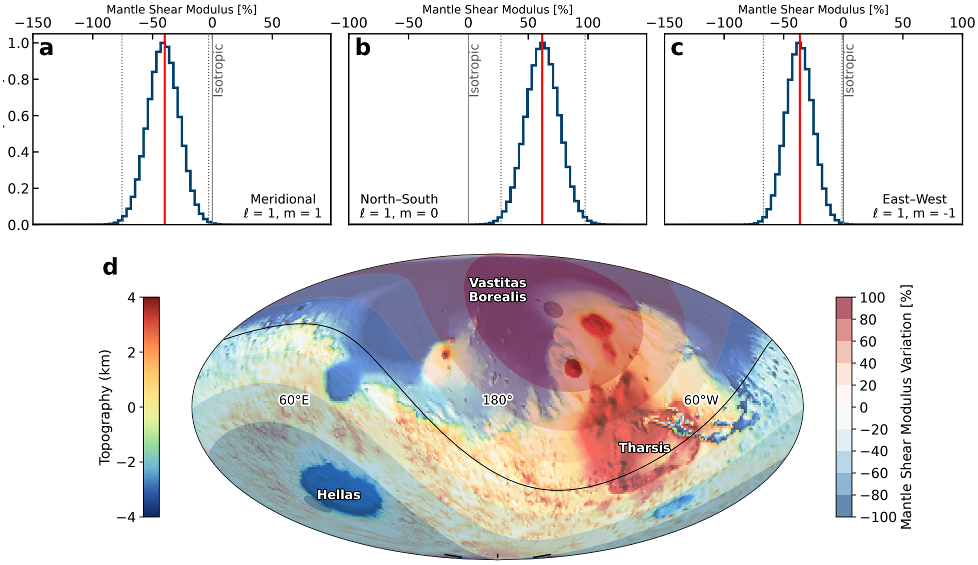

Fig. 2 Tidal tomography of the Martian mantle. (**a**–**c**) Histograms of inverted coefficient values that describe internal hemispheric (degree-1) variations in shear modulus (in percent relative to the bulk value) for the Martian mantle (50-1,560 km depth). Meridional, North-South, and East-West labels denote order−1, order−0, and order−-1 variations respectively. Dotted lines indicate 0.3 and 99.7% percentiles (that is, 3-σ confidence bounds) and the red solid lines indicate maximum a-posteriori solutions (that is, the location of the absolute maximum of posterior distributions). A full list of derived harmonic coefficients describing 3D structure is shown in Extended Data Table 3. (**d**) Plot of Martian topography (MGS-M-MOLA-5-IEGDR[55], red–orange–yellow–green–blue colormap) overlain by semi-transparent map of the combination of maximum a-posteriori solutions for degree-1 variations in mantle shear modulus shown in panels a–c (red–blue colormap). Black contour indicates the trace of the zero value of shear modulus variations. Approximate locations of Tharsis, Vastitas Borealis, and Hellas basin are indicated. Map is shown in Mollweide projection.

Thermal Anomaly Beneath Mars's Highlands

Our modeling suggests that Mars's anomalous degree-3 gravity field arises from a substantial, >20% lateral variation in the mantle's effective shear modulus at the seasonal timescale. What could generate such a large contrast? At a given pressure, the rigidity of mantle rock depends on both temperature and composition. At seismic timescales, crystalline temperature differences would need to exceed an unrealistically large >1000 K to produce observed shear modulus variations[4]. However, when extended to the Martian annual period (see Methods and Extended Data Fig. 6), the effective shear modulus of olivine becomes approximately 15–20 times more sensitive to temperature[35]. As such, recovered shear-modulus variations can primarily be explained by a hemispheric temperature anomaly of approximately 200–400 K in the present-day Martian mantle (Fig. 3, see Methods). Thermal modeling also suggests that the insulating effect of the thicker crust in the Southern highlands can result in a hemispheric temperature contrast >200 K (Fig. 3f of[15]), consistent with our results. Mars's center-of-mass–center-of-figure (COM–COF) offset also limits the potential compositional component (e.g., iron, water content) of asymmetries since, in isolation, such differences (and their associated density structure) would need to produce an offset that is approximately 50 times larger than observations[36] to account for the inferred shear modulus variations. Even so, our models allow for up to 5% iron enrichment (that is, variation in Forsterite-Fayalite mol fraction or ΔFo-Fa) within the Southern highlands' mantle (Fig. 3).

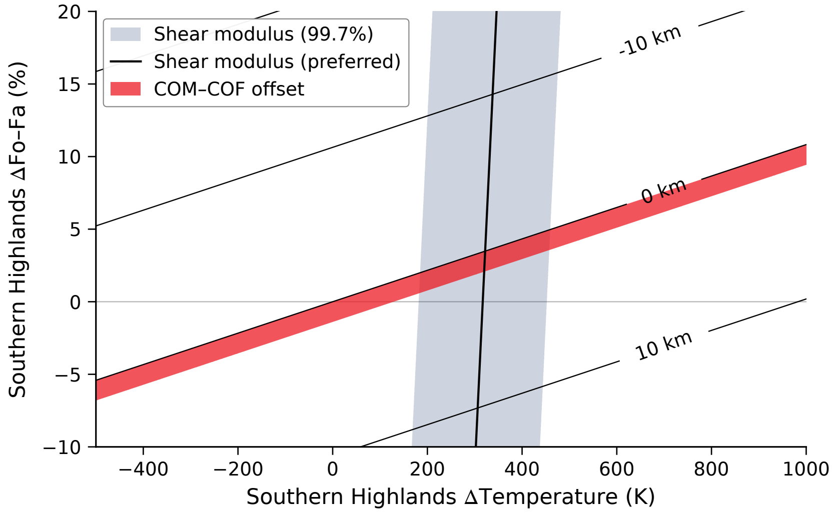

Fig. 3 Relationship between temperature, composition, and inferred shear modulus variations in the Martian mantle. Shaded regions indicate the constrained ranges of the inferred Martian effective hemispheric shear modulus variation and the impact of mantle structure on the center-of-mass center-of-figure (COM–COF) offset as a function of Southern Highlands mantle temperature anomaly and fayalite–forsterite mol fraction contrast (Fa–Fo) (for details regarding calculations, see Methods). Values are projected onto a degree-1 pattern with poles centered at 45°N 138°W (Northern lowlands) and 45°S 42°E (Southern highlands). Black contours indicate COM-COF offsets at 10 km intervals. Since the COM–COF offset is sensitive to the structure of both the crust and mantle, our modelled 0–1.31 km range of values accounts for the possibility of (i) an anomalous COF that is fully attributable to elevated topography over the Southern highlands (paired with Airy or Pratt compensation of this structure at depth) or an anomalous COM arising from a relatively dense crust over the Northern Lowlands (i.e., the 0 km bound) [11;18;36], (ii) an anomalous COM that is solely attributable to mantle density variations (i.e., the 1.31 km bound) and (iii) intermediate cases. The blue shaded area and thick solid black line respectively denote the 99.7% confidence bounds and preferred value for the overall shear modulus difference of $81 \pm 60\%$ inferred from gravity data in this work (see Fig. 2). By identifying overlapping portions of parameter space that satisfy both the 99.7% range of inferred shear modulus variation and COM–COF offset, we infer that hemispheric asymmetries can be explained by a temperature anomaly of 200–400 K and an iron enrichment of up to 5% in the Southern Highlands mantle.

Mantle heterogeneities may preserve signatures of, and thus provide independent constraints on, geodynamic processes that influence the evolution of the crustal dichotomy. We consider three such candidate processes: a giant impact, spontaneous degree-1 upwelling (that persists into the present-day), and enhanced thermal insulation or radiogenic heating of the Southern highlands mantle by a thick overlying crust. Spontaneous degree-1 upwelling or thermal insulation would produce a primarily thermal mantle anomaly[12–15] as well as potential secondary compositional signatures through decompression melting below the lithosphere[12–15]. However, enhanced melt extraction in these scenarios would deplete the Southern highlands mantle in iron[12;37], opposite to the observations (Fig. 3). By contrast, a giant impact is (in isolation) not expected to result in a long-term secular variation in temperature of several hundred Kelvin over a given hemisphere[38]. A hybrid scenario could resolve this mismatch. For example, upon the formation of the Northern lowland crust from the Borealis impact, the Northern hemisphere mantle is first depleted in iron[37] leaving the Southern mantle relatively enriched. The resultant thicker Southern crust could also trigger preferential thermal insulation[15] or degree-1 upwelling[39] below Mars's highlands (the latter would be favoured absent variations in crustal thickness or radiogenic material abundance[18]), increasing this region's present-day temperature (Figs. 3, 4).

Temperature variations may also influence the dissipative properties of Mars's mantle. For example, comparisons of low-frequency Marsquakes detected by the *InSight* lander indicate substantially lower quality factors ($Q \sim 500$) for events originating in the nearby Terra Cimmeria region of the Southern highlands than for events from Cerberus Fossae in the Northern lowlands ($Q \sim$ 800–2,000)[20]. These differences in attenuation can be attributed to lateral variations in the temperature of the mantle of a few hundred Kelvin (Fig. 4 of[20]). A warm Southern highlands' mantle might also result in localized melting[14] which could reduce the 200–400 K temperature anomaly required to explain gravity field observations (Fig. 3). However, the Q

values inferred for the Southern highlands remain well above those expected for partially molten olivine ($Q \sim 100$ or lower)[20]. Even so, future electromagnetic sounding measurements (for example,[40]) could resolve whether the inferred thermal anomaly in the Southern Highlands mantle is associated with isolated magma pockets or with a more continuous molten layer at depth (e.g.,[14;32]).

The preferential magnetization of the Southern highlands crust[19] may also reflect the effects of a laterally heterogeneous interior. For example, upwelling beneath the Southern Highlands may have heated the overlying crust above Curie temperatures while Mars's ancient dynamo was active (4.5–4.1 Gya)[41]. These temperatures may have subsequently fallen below Curie temperatures prior to the cessation of the dynamo, allowing affected portions of the Southern highlands to acquire their present-day remanent magnetization[13;42]. Alternatively, elevated heat flow at the core-mantle boundary (and in the overlying mantle) may have regionally enhanced convection in Mars's outer core resulting in a stronger dynamo below the Southern highlands[43]. Inferred asymmetries in mantle structure may therefore constitute a present-day remnant of geodynamic processes associated with the generation of Mars's early dynamo (see Fig. 4).

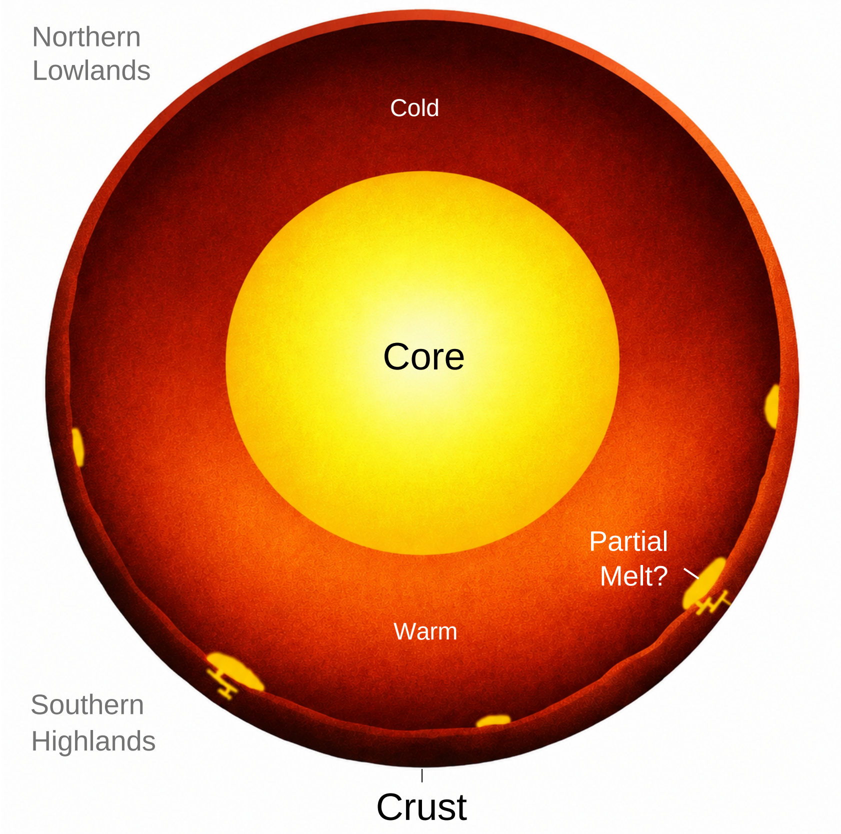

Fig. 4 Conceptual model of Mars's interior structure as inferred in the present study. Measured temporal variations in degree-3 gravity indicate a thermal anomaly within the mantle beneath the Southern highlands (light yellow to orange regions outside of the core). This anomaly may promote partial melting below Mars's lithosphere which ascends and stalls in the crust prior to reaching the surface[14]. This upwelling could result in thickening and enhanced magnetization across Mars's Southern highlands' crust. In contrast, the mantle beneath the Northern lowlands is comparatively cool (dark red to brown regions). Illustration is not to scale.

Volcanism and Future Measurements

Although melt is not required by our results (Fig. 3), some thermal models predict that elevated temperatures in the Southern Highlands' mantle would increase magma production in this region[14]. Such pockets of deep-seated melt are expected to ascend and erupt onto the surface over timescales of a few Myr[44] (see Methods). Yet recent (tens of Myr) volcanic activity is confined to Cerberus Fossae in the North[45]. We propose two potential solutions to this apparent paradox. The first is that the thicker (and potentially lower-density[46]) crust in the Southern Highlands may present a barrier to melt ascent. Under this scenario, melt would stall in the mid-crust and generate local intrusive features (see Fig. 4). These intrusions would be difficult to detect in surface images but may be resolved from very high-resolution ($\ell > 300$) measurements of Mars's static gravity field[47]. The second solution is that melt ascent and eruption requires a background extensional stress field[48]. Tectonic features in the Southern highlands are dominantly compressional (for example,[49]), as expected from Mars's slow cooling. In contrast, Cerberus Fossae is a region undergoing localized extension[50]. In any case, the petrology of volcanic rocks sampled from different locations over Mars's crust could constrain the spatial differences in mantle potential temperature implied by our results[51].

Tidal tomography—or the inference of lateral variations in interior structure from a body's time-variable response to tidal forcing—has been used to probe the mantle of Earth[2] and, more recently, the Moon[4]. Here, we use nearly two decades of precise spacecraft tracking data to extend this approach to Mars. Future missions with dedicated gravity experiments (similar to GRACE for Earth[52] or GRAIL for the Moon[53]) could resolve similar (or finer) variations in Martian mantle structure over much shorter mission durations[54]. In the future, these techniques may also be applied to other planetary bodies that exhibit pronounced low-order asymmetries in structure, including Ganymede, Mercury, Io, and Enceladus. Because tidal tomography largely relies on remote measurements, it represents a powerful tool for future missions seeking to characterize the interiors of planetary bodies without landed spacecraft.

References

[1] Hoolst, T. V., Dehant, V., Roosbeek, F. & Lognonné, P. Tidally induced surface displacements, external potential variations, and gravity variations on mars. *Icarus* **161**, 281–296 (2003). URL https://doi.org/10.1016/S0019-1035(02)00045-3.

[2] Lau, H. C. P. *et al.* Tidal tomography constrains earth's deep-mantle buoyancy. *Nature* **551**, 321–326 (2017).

[3] Berne, A., Simons, M., Keane, J. T., Leonard, E. J. & Park, R. S. Jet activity on enceladus linked to tidally driven strike-slip motion along tiger stripes. *Nature Geoscience* **17**, 385–391 (2024).

[4] Park, R. S. *et al.* Thermal asymmetry in the moon's mantle inferred from monthly tidal response. *Nature* **641**, 1188–1192 (2025).

[5] Smith, D. E. *et al.* The gravity field of mars: Results from Mars Global Surveyor. *Science* **286**, 94–97 (1999).

[6] Saunders, R. S. *et al.* 2001 mars odyssey mission summary. *Space Science Reviews* **110**, 1–36 (2004).

[7] Zuber, M. T. *et al.* Mars reconnaissance orbiter radio science gravity investigation. *Journal of Geophysical Research: Planets* **112**, – (2007).

[8] Zhong, S., Qin, C., A, G. & Wahr, J. Can tidal tomography be used to unravel the long-wavelength structure of the lunar interior. *Geophysical Research Letters* **39**, L24201 (2012).

[9] Qin, C., Zhong, S. & Wahr, J. Elastic tidal response of a laterally heterogeneous planet: a complete perturbation formulation. *Geophysical Journal International* **207**, 89–110 (2016).

[10] Rovira-Navarro, M., Matsuyama, I. & Berne, A. A spectral method to compute the tides of laterally heterogeneous bodies. *The Planetary Science Journal* **5**, 129 (2024). URL https://doi.org/10.3847/PSJ/ad381f.

[11] Wieczorek, M. A. & Zuber, M. T. Thickness of the Martian crust: Improved constraints from geoid-to-topography ratios. *Journal of Geophysical Research: Planets* **109**, E01009 (2004).

[12] Zhong, S. & Zuber, M. T. Degree-1 mantle convection and the crustal dichotomy on mars. *Earth and Planetary Science Letters* **189**, 75–84 (2001).

[13] Roberts, J. H. & Zhong, S. Degree-1 convection in the martian mantle and the origin of the hemispheric dichotomy. *Journal of Geophysical Research* **111** (2006).

[14] Gibet, V. B., Michaut, C., Wieczorek, M. & Lognonné, P. A positive feedback between crustal thickness and melt extraction for the origin of the martian dichotomy. *Journal of Geophysical Research: Planets* **127**, e2022JE007472 (2022).

[15] Plesa, A. C. *et al.* The thermal state and interior structure of mars. *Geophysical Research Letters* **45**, 12198–12209 (2018). URL https://doi.org/10.1029/2018GL080728.

[16] Andrews-Hanna, J. C., Zuber, M. T. & Banerdt, W. B. The borealis basin and the origin of the martian crustal dichotomy. *Nature* **453**, 1212–1215 (2008).

[17] Kim, D. *et al.* Global crustal thickness revealed by surface waves orbiting Mars. *Geophysical Research Letters* **50**, e2023GL103482 (2023).

[18] Wieczorek, M. A. *et al.* Insight constraints on the global character of the martian crust. *Journal of Geophysical Research: Planets* **127**, e2022JE007298 (2022). URL https://doi.org/10.1029/2022JE007298.

[19] Lillis, R. J., Frey, H. V. & Manga, M. Rapid decrease in martian crustal magnetization in the noachian era: Implications for the dynamo and climate of early mars. *Geophysical Research Letters* **35**, L14203 (2008). URL https://doi.org/10.1029/2008GL034338.

[20] Sun, X. & Tkalčić, H. Constraints on the origin of the martian dichotomy from southern highlands marsquakes. *Geophysical Research Letters* **51**, e2024GL110921 (2024). URL https://doi.org/10.1029/2024GL110921.

[21] Jakosky, B. M. *et al.* Loss of the martian atmosphere to space: Present-day loss rates determined from maven observations and integrated loss through time. *Icarus* **315**, 146–157 (2018).

[22] Hurowitz, J. A. *et al.* Redox-driven mineral and organic associations in jezero crater, mars. *Nature* **645**, 332–336 (2025).

[23] Reese, C. C., Orth, C. P. & Solomatov, V. S. Impact megadomes and the origin of the martian crustal dichotomy. *Icarus* **213**, 433–442 (2011).

[24] Cheng, K. W. *et al.* Mars's crustal and volcanic structure explained by southern giant impact and resulting mantle depletion. *Geophysical Research Letters* (2024).

[25] Marinova, M. M., Aharonson, O. & Asphaug, E. Mega-impact formation of the mars hemispheric dichotomy. *Nature* **453**, 1216–1219 (2008). URL https://doi.org/10.1038/nature07070.

[26] Konopliv, A. S. *et al.* Mars high resolution gravity fields from mro, mars seasonal gravity, and other dynamical parameters. *Icarus* **211**, 401–428 (2011).

[27] Hemingway, D. J. & Mittal, T. Enceladus's ice shell structure as a window on internal heat production. *Icarus* **332**, 111–131 (2019). URL https://doi.org/10.1016/j.icarus.2019.03.011.

[28] Genova, A. *et al.* Seasonal and static gravity field of Mars from MGS, Mars Odyssey and MRO radio science. *Icarus* **272**, 228–245 (2016).

[29] Stähler, S. C. *et al.* Seismic detection of the martian core. *Science* **373**, 443–448 (2021). URL https://www.science.org/doi/10.1126/science.abi7730.

[30] Bi, H. *et al.* Seismic detection of a 600-km solid inner core in Mars. *Nature* **645**, 67–72 (2025).

[31] Smith, D. E., Zuber, M. T., Haberle, R. M., Rowlands, D. D. & Murphy, J. R. The Mars seasonal CO_2 cycle and the time variation of the gravity field: A general circulation model simulation. *Journal of Geophysical Research* **104**, 1885–1896 (1999).

[32] Samuel, H. *et al.* Geophysical evidence for an enriched molten silicate layer above mars's core. *Nature* **622**, 712–717 (2023). URL https://www.nature.com/articles/s41586-023-06601-8.

[33] Andrews-Hanna, J. C., Zuber, M. T. & Banerdt, W. B. The borealis basin and the origin of the martian crustal dichotomy. *Nature* **453**, 1212–1215 (2008).

[34] Broquet, A. & Andrews-Hanna, J. C. Geophysical evidence for an active mantle plume underneath elysium planitia on mars. *Nature Astronomy* **7**, 160–169 (2023). URL https://doi.org/10.1038/s41550-022-01836-3.

[35] Jackson, I. & Faul, U. H. Grainsize-sensitive viscoelastic relaxation in olivine: Towards a robust laboratory-based model for seismological application. *Physics of the Earth and Planetary Interiors* **183**, 151–163 (2010).

[36] Smith, D. E. *et al.* Mars orbiter laser altimeter: Experiment summary after the first year of global mapping of mars. *Journal of Geophysical Research: Planets* **106**, 23689–23722 (2001).

[37] Shaw, D. M. Trace element fractionation during anatexis. *Geochimica et Cosmochimica Acta* **34**, 237–243 (1970).

[38] Ruedas, T. & Breuer, D. On the relative importance of thermal and chemical buoyancy in regular and impact-induced melting in a Mars-like planet. *Journal of Geophysical Research: Planets* **122**, 1554–1579 (2017).

[39] Citron, R. I., Manga, M. & Tan, E. A hybrid origin of the martian crustal dichotomy: Degree-1 convection antipodal to a giant impact. *Earth and Planetary Science Letters* **491**, 58–66 (2018).

[40] Civet, F. & Tarits, P. Electrical conductivity of the mantle of mars from MGS magnetic observations. *Earth, Planets and Space* **66**, 85 (2014).

[41] Ruiz, J. The very early thermal state of terra cimmeria: Implications for magnetic carriers in the crust of mars. *Icarus* **203**, 173–179 (2009). URL https://doi.org/10.1016/j.icarus.2009.05.021.

[42] Nimmo, F. & Stevenson, D. J. Influence of early plate tectonics on the thermal evolution and magnetic field of mars. *Journal of Geophysical Research: Planets* **105**, 11969–11979 (2000).

[43] Yan, C. *et al.* An ancient martian dynamo driven by hemispheric heating: Effect of thermal boundary conditions. *The Planetary Science Journal* **4**, 11 (2023).

[44] McKenzie, D. Some remarks on the movement of small melt fractions in the mantle. *Earth and Planetary Science Letters* **95**, 53–72 (1989).

[45] Berman, D. C. & Hartmann, W. K. Recent fluvial, volcanic, and tectonic activity on the cerberus plains of mars. *Icarus* **159**, 1–17 (2002).

[46] Phillips, M. S. *et al.* Widespread ancient anorthosites in the lower crust of mars. *Communications Earth & Environment* **6**, 1026 (2025).

[47] Losarcos, J. M. & Dombard, A. J. Lava tubes on Earth, the Moon, and Mars: Detection, evolution, and exploration potential. *Space Science Reviews* **221**, 127 (2025).

[48] Solomon, S. C. On volcanism and thermal tectonics on one–plate planets. *Geophysical Research Letters* **5**, 461–464 (1978).

[49] Andrews-Hanna, J. C. & Broquet, A. The history of global strain and geodynamics on mars. *Icarus* **395**, 115476 (2023).

[50] Stähler, S. C. *et al.* Tectonics of cerberus fossae unveiled by marsquakes. *Nature Astronomy* **6**, 1376–1386 (2022).

[51] Baratoux, D., Toplis, M. J., Monnereau, M. & Gasnault, O. Thermal history of Mars inferred from orbital geochemistry of volcanic provinces. *Nature* **472**, 338–341 (2011).

[52] Wahr, J., Swenson, S., Zlotnicki, V. & Velicogna, I. Time-variable gravity from grace: First results. *Geophysical Research Letters* **31**, L11501 (2004).

[53] Park, R. S., Vaughan, A. T. *et al.* Gravity imaging radio observer (giro) for planetary science and mission opportunities. *The Planetary Science Journal* **6**,

127 (2025).
[54] Keane, J. T. *et al.* *Next-generation planetary geodesy: Results from the 2021 keck institute for space studies workshops.* In *53rd Lunar and Planetary Science Conference*, LPI Contribution No. 2678, 1622 (2022). URL https://ui.adsabs.harvard.edu/abs/2022LPICo2678.1622K.
[55] Smith, D. E. & Team, M. S. Mgs-m-mola-5-iegdr-l3-v1.0: Ieg100_a ascii topography / radius table. NASA Planetary Data System (PDS), Geosciences Node (1999). URL https://pds-geosciences.wustl.edu/mgs/mgs-m-mola-5-iegdr-l3-v1/mgsl_2xxx/data/ieg100_a.tab. Initial Experiment Gridded Data Record (IEGDR), 1° × 1° grid, ASCII table format.

Methods

Modeling the Time-Varying Gravity Field

The gravitational potential for Mars, $U(r, \lambda, \phi)$, can be expressed as a sum over 4π-normalized spherical harmonic coefficients $C_{\ell m}$ and $S_{\ell m}$:

$$U(r, \lambda, \phi) = \frac{GM}{r}\left[1 + \sum_{\ell=2}^{\infty}\left(\frac{R_m}{r}\right)^{\ell}\sum_{m=0}^{\ell}\left(C_{\ell m}\cos m\lambda + S_{\ell m}\sin m\lambda\right)\, P_{\ell m}(\sin\phi)\right], \tag{1}$$

where G is the gravitational constant, M is the mass of Mars, R_m is a reference radius, $P_{\ell m}$ are fully normalized associated Legendre functions, r is the radial distance from the planet's center, λ is the planetocentric longitude, and ϕ is the planetocentric latitude. The gravity field is expressed in Mars's body-fixed frame (as defined in[26]), centered at the planet's center of mass, so that the degree-1 coefficients vanish by definition. To describe the temporal variability of the Martian gravity field, periodic terms are introduced into the normalized coefficients. This formulation, implemented within the GEODYN II orbit determination framework[56], allows the harmonic coefficients $C_{\ell m}$ and $S_{\ell m}$ to vary in time to account for periodic mass redistribution. This time-dependent expansion is written as:

$$\begin{aligned} C_{\ell m}(t) &= \bar{C}_{\ell m} + \sum_{k=1}^{3} \left[\Delta C_{\ell m}^{A,(k)} \cos(\omega^{(k)} t) + \Delta C_{\ell m}^{B,(k)} \sin(\omega^{(k)} t) \right], \\ S_{\ell m}(t) &= \bar{S}_{\ell m} + \sum_{k=1}^{3} \left[\Delta S_{\ell m}^{A,(k)} \cos(\omega^{(k)} t) + \Delta S_{\ell m}^{B,(k)} \sin(\omega^{(k)} t) \right], \end{aligned} \tag{2}$$

where $\bar{C}_{\ell m}, \bar{S}_{\ell m}$ are static (that is, not changing with time) components of the Martian gravity field, $\omega^{(k)}$ represents the angular frequency of the k-th periodic component where $k = 1, 2, 3$ respectively correspond to the Martian annual (or seasonal), semi-annual, and triannual periods, and t is time following the reference epoch (J2000). The amplitudes $\Delta C_{\ell m}^{A,(k)}$, $\Delta S_{\ell m}^{A,(k)}$, $\Delta C_{\ell m}^{B,(k)}$, and $\Delta S_{\ell m}^{B,(k)}$ represent the cosine and sine coefficients of the k-th harmonic component, which together describe the temporal modulation of each spherical harmonic term at the modeled frequencies. For this work, we specifically extract coefficients at the Martian annual period for use in tidal tomography inversions (that is, $\Delta C_{\ell m}^{A,B} \equiv \Delta C_{\ell m}^{A,B,(k=1)}$ and $\Delta S_{\ell m}^{A,B} \equiv \Delta S_{\ell m}^{A,B,(k=1)}$, $\omega \equiv \omega_1 = 1.058 \times 10^{-7}$ rad/s, $t = \frac{\omega}{2\pi} n + t_0$ (n is an integer) are yearly intervals after the J2000 epoch t_0).

Gravity Field Inversion

We co-estimate parameters $\Delta C_{\ell m}^{A,B}$ and $\Delta S_{\ell m}^{A,B}$ up to $\ell = 3$ along with static coefficients $\bar{C}_{\ell m}$ and $\bar{S}_{\ell m}$ up to $\ell = 120$ in Equation 2 through our gravity inversion procedure. To do so, we reprocess Earth-based radiometric (X-band) Doppler tracking data acquired by the DSN from the MGS, ODY, and MRO missions. The dataset spans approximately sixteen years, corresponding to about one and a half solar cycles[28]. Following an initial step of correcting for non-gravitational effects on spacecraft acceleration, we minimize residuals between predicted spacecraft range rate values (that is, for an iteratively updated gravity field) and range rate observations. These steps are described in detail below.

Estimation of the gravitational coefficients was achieved through a batch least-squares analysis using orbital arcs of 2.5-8 days, with the arc length varying according to the mission phase. For each arc, partial derivatives of the Doppler observables were computed with respect to the estimated parameters, and a global simultaneous inversion of all arcs and all parameters at once was performed to minimize the residuals between the observed and modeled tracking data. Our analysis represents an extension of previous analyses focused primarily on evaluating the temporal evolution of the zonal terms [28;57]. Results for the degree-3 and degree-2 zonal terms do not change beyond 2–σ uncertainty when adding the non-zonal terms. Moreover, estimating only degree-3 time-varying terms or explicitly including non-zonal degree-2 terms does not significantly change degree-3 terms inferred from our analysis. As an additional check, we performed a sensitivity analysis of post-fit residuals and empirical accelerations to the inclusion of the degree-3 time-variable gravity field using 2017 tracking data not used in the gravity field determination. The RMS of fit for these independent test arcs improves only marginally ($< 1\%$) upon inclusion of the degree-3 time-varying terms (Extended Data Fig. 7a). This is expected: long-period tidal parameters are constrained by stacking many years of data, so no individual arc is expected to show a marked improvement in fit. Similarly, the a posteriori amplitudes of the empirical accelerations change only marginally and without a systematic trend when the degree-3 time-varying terms are included (Extended Data Fig. 7b,c).

We correct for the contribution of the atmosphere on the Martian gravity field. To do so, we incorporate a time series of spherical harmonic coefficients representing the atmospheric load within the orbit determination procedure (see Eq. 4 in [28]). At each epoch, we expand the surface pressure $P_s(\lambda, \phi, t)$ provided by the Mars Climate

Database (MCD[58]) and include the solid-body response to this surface load through degree-dependent loading Love numbers k'_ℓ:

$$\begin{aligned}\Delta C^{\mathrm{atm}}_{\ell m}(t) &= \frac{3\,(1+k'_\ell)}{4\pi\,\bar{\rho}\,g\,R_m\,(2\ell+1)} \oint P_s(\lambda,\phi,t)\,P_{\ell m}(\sin\phi)\,\cos(m\lambda)\,d\Omega,\\ \Delta S^{\mathrm{atm}}_{\ell m}(t) &= \frac{3\,(1+k'_\ell)}{4\pi\,\bar{\rho}\,g\,R_m\,(2\ell+1)} \oint P_s(\lambda,\phi,t)\,P_{\ell m}(\sin\phi)\,\sin(m\lambda)\,d\Omega,\end{aligned} \tag{3}$$

where $\bar{\rho}$ is Mars's mean density, g is Mars's mean surface gravity, $P_{\ell m}(\sin\phi)$ are the same fully normalized associated Legendre functions used in Equation 1, $P_s(\lambda,\phi,t)$ is the instantaneous surface pressure field, and $d\Omega = \cos\phi\,d\lambda\,d\phi$ is the element of solid angle on the unit sphere. The integrals project $P_s(\lambda,\phi,t)$ onto the cosine and sine basis of Equation 2, and the factor $(1+k'_\ell)$ accounts for the deformation of the solid planet under this surface load. The loading Love numbers k'_ℓ are computed for a spherically symmetric, self-gravitating 1D elastic Mars using the semi-analytic method described in[59]. The radially stratified reference interior used for this calculation is described in Extended Data Table 2 and yields $k'_2 = -0.14126$ and $k'_3 = -0.09109$. We note that atmospheric surface loads at $\ell = 2$ and $\ell = 3$ are comparable in magnitude, so mode coupling between harmonics (that is $\ell = 2$ to $\ell = 3$) driven by lateral heterogeneity negligibly impact k'_2 and k'_3. For consistency, we additionally tested changes to the within-harmonic (diagonal) response of a laterally heterogeneous Martian interior with degree-1, order-$(-1,0,1)$ shear-modulus variations of 36%, 60%, 42% in the mantle (see Figure 2) using a finite-element code[3;60–66]. This model returns k'_2 and k'_3 values that agree with parameters from the 1D reference model to within $< 1\%$. We additionally test the impact of varying k'_ℓ by 200% and 0% (relative to baseline values, '0%' indicates a case with no deformational response to surface loads) on inversion results (Fig. 2), and find that these changes to assumed k'_ℓ impact the median of recovered degree-1 shear modulus coefficient values by $< 10\%$ (see Extended Data Fig. 2).

The spherical harmonic expansions for Mars's atmosphere in Equation 3 are evaluated at 2-hour intervals to capture diurnal and semidiurnal components, and are included in the dynamical modeling of each spacecraft. The MCD and the Drag Temperature Model-Mars (DTM-Mars[67]) used for modelling non-gravitational forces (see below) apply to distinct altitude regimes (the lower atmosphere and the thermosphere, respectively) but share a common calibration against Mars atmospheric observations (and physical assumptions) and are therefore internally consistent for this analysis. The final retrieved static and time-varying gravity fields corrected for the atmosphere, given in Eqs. 1,2 and Table 1 and shown as blue bars in Fig. 1, are therefore representative of the solid-body response only. Variations in the retrieved $\Delta C_{\ell m}^{A,B}$ and $\Delta S_{\ell m}^{A,B}$ across these permutations remain stable on multi-year timescales (Extended Data Fig. 1a) and are generally smaller than the observational uncertainties reported in Fig. 1a, Table 1, and Extended Data Table 1 (Extended Data Fig. 1b); we correspondingly do not propagate these variations into the uncertainties for the atmosphere-corrected observations used as constraints on tidal tomography inversions. We do not correct for the seasonal condensation of atmospheric CO_2 onto the surface (or associated deformational response) for non-zonal harmonics since related gravity perturbations, from both mass redistribution and surface deflection, are expected to be a few orders of magnitude smaller than the observations in Table 1 or Extended Data Table 1[59;68].

Past studies have tested the impact of several additional modelling choices for the Martian atmosphere, including the incident solar flux (parameterized via the proxy quantity 'extreme ultraviolet radiation' or EUV) and the the level of atmospheric dust opacity[28;57]. For example,[28] find that whereas the incident solar flux has a monotonic impact on gravity coefficients, dust opacity tends to amplify the impact of changes in incident solar flux on Mars's time-variable gravity coefficients. Therefore, as an additional check, we reprocessed the atmospheric contributions from

Equation 3 to compare our baseline model (an average solar flux scenario, 'Avg EUV', $F_{10.7} \approx 130$ sfu[58]) against endmember scenarios drawn from the Mars Climate Database: (i) a cold atmosphere case with minimum solar flux ($F_{10.7} \approx 70$ sfu or solar flux units where 1 sfu $= 10^{-22}$ W m^{-2} Hz^{-1}[58]) combined with dust-storm conditions (column-integrated visible optical depth $\tau \gtrsim 5$[69]) or 'Cold min EUV dust', and (ii) a warm atmosphere case with maximum solar flux ($F_{10.7} \approx 200$ sfu[58]) combined with the same dust opacity or 'Warm max EUV dust'. These differences between atmospheric models, when applied as corrections to the atmosphere-corrected observations shown in Fig. 1, propagate into $\leq$20% shifts in the inferred posterior distributions of degree-1 mantle shear modulus relative to our nominal inversion (Extended Data Fig. 2). The most substantial shifts (relative to the nominal case) occur for the 'Cold min EUV dust' scenario, though, recovered posteriors for this case indicate a north-south pattern which still broadly aligns with the structure of the crustal dichotomy (degree-1 order-0 and degree-1 order-1 variations remain significant at 3-σ and 2-σ levels, respectively).

We correct for non-gravitational forces on each spacecraft with a detailed forward model of the non-conservative perturbations. To this end, we represent each spacecraft as a multi-panel body and assign thermo-optical properties to movable surfaces such as the high-gain antenna and solar arrays. We predict the thermospheric density along each orbit with DTM-Mars[67] updated for the revised evolution of the major atmospheric constituents[70]. To absorb any residual mismodeling, we additionally co-estimate small periodic accelerations in the along- and cross-track directions at frequencies tied to the orbital period, following[28]. We note that though tidal forcing is theoretically stronger at diurnal frequencies than at the seasonal period[1], the higher-frequency components of Mars's time-variable gravity are also the most susceptible to residual non-gravitational errors. Estimated empirical accelerations therefore largely absorb diurnal tidal signals together with the perturbations they target[28;57].

For this reason, we do not attempt to recover diurnal tidal signals and restrict our analysis to the annual gravity field variations.

Modeling Mars's Tidal Deformation

We directly model the impact of tidal deformation associated with Sun–Mars tides on coefficients $\Delta C_{\ell m}$ and $\Delta S_{\ell m}$ according to (superscript 'p' denotes 'predicted'):

$$\Delta C^p_{\ell m} - i\,\Delta S^p_{\ell m} = f^p(t) \tag{4}$$

where:

$$\begin{aligned} f^p(t) = \frac{1}{N_{\ell m}} \sum_{\ell'=2}^{3} \sum_{m'=0}^{\ell'} \frac{1}{2\ell'+1} \frac{GM_S}{GM} \frac{R^{\ell'+1}}{r_S^{\ell'+1}} P_{\ell' m'}(\sin\phi_S) \\ \times \Big[(K^{\ell,m}_{\ell',m'} \cos(m'\lambda_S) + K^{\ell,m}_{\ell',-m'} \sin(m'\lambda_S)) \\ - i\,(K^{l,-m}_{\ell',m'} \cos(m'\lambda_S) + K^{l,-m}_{\ell',-m'} \sin(m'\lambda_S)) \Big]. \end{aligned} \tag{5}$$

In Equation 5, M_S is the mass of the Sun and (λ_S, ϕ_S, r_S) represent solar longitude, latitude, and distance in Mars's body-fixed frame. We evaluate (λ_S, ϕ_S, r_S) based on solar and Martian ephemerides extracted from NASA's Planetary Data System evaluated over the mission durations of the MGS, ODY, and MRO spacecraft. Note that Equation 5 accounts for tides which arise from both Mars's 0.0934 eccentricity and 25.2° spin-axis obliquity relative to the Sun through the impact of these orbital parameters on variations in λ_S, ϕ_S, r_S. $N_{\ell m}$ is the normalization factor:

$$N_{\ell m} = \sqrt{\frac{(\ell - m)!\,(2 - \delta_{0m})(2\ell + 1)}{(\ell + m)!}} \tag{6}$$

$K^{\ell,m}_{\ell',m'}$ in Equation 5 denote 'Extended Love numbers' (distinct from traditional Love numbers $k_{\ell m}$) that represent coupling between forcing at one harmonic (l', m') and the gravitational response to this forcing at another harmonic (l, m) for a given interior structure. We compute $K^{\ell,m}_{\ell',m'}$ using the semi-analytic spectral method LOV3D [10] (see also[71;72]), which solves mass conservation, momentum and Poisson's equations in the Fourier domain for a laterally heterogeneous body subject to tidal loading[3;60–63]. Given $K^{\ell,m}_{\ell',m'}$, we compute $\Delta C^{A,B,p}_{\ell m}$ and $\Delta S^{A,B,p}_{\ell m}$ by evaluating $f^p(t)$ in Equation 5 and then projecting this quantity into cosine and sine functions evaluated over the Martian annual period:

$$\begin{aligned}
\Delta C^{A,p}_{\ell m} &= \Re\left(\frac{\omega}{2\pi}\int_{t_{start}}^{t_{end}} f^p(t)\cos(\omega t)dt\right)\\
\Delta C^{B,p}_{\ell m} &= \Re\left(\frac{\omega}{2\pi}\int_{t_{start}}^{t_{end}} f^p(t)\sin(\omega t)dt\right)\\
\Delta S^{A,p}_{\ell m} &= \Im\left(-\frac{\omega}{2\pi}\int_{t_{start}}^{t_{end}} f^p(t)\cos(\omega t)dt\right)\\
\Delta S^{B,p}_{\ell m} &= \Im\left(-\frac{\omega}{2\pi}\int_{t_{start}}^{t_{end}} f^p(t)\sin(\omega t)dt\right)
\end{aligned} \tag{7}$$

.

Note that Equation 7 captures only the solid-body tidal response. However, zonal coefficients are additionally sensitive to seasonal CO_2 exchange between the polar caps, which we model separately:

$$\Delta C^{A,B,p}_{\ell 0} = \Delta C^{A,B,p,\,\mathrm{solid}}_{\ell 0} + \Delta C^{A,B,p,\,\mathrm{poles}}_{\ell 0}, \tag{8}$$

where $\Delta C^{A,B,p,\,\mathrm{solid}}_{\ell 0}$ is computed from Equation 7, and the polar-cap contribution $\Delta C^{A,B,p,\,\mathrm{poles}}_{\ell 0}$ is computed by representing the seasonal mass exchange as time-varying point masses $\Delta m_N(t)$ and $\Delta m_S(t)$ located at the north and south rotation poles. For point masses on the rotation axis, the corresponding (4π-normalized) coefficient is:

$$\Delta C^{\mathrm{poles}}_{\ell 0}(t) = \frac{1}{M\sqrt{2\ell+1}}\left[\Delta m_N(t) + (-1)^{\ell}\,\Delta m_S(t)\right], \tag{9}$$

which for the degree-2 and degree-3 zonal terms reduces to

$$\Delta C_{20}^{\text{poles}}(t) = \frac{\Delta m_N(t) + \Delta m_S(t)}{M\sqrt{5}}, \qquad \Delta C_{30}^{\text{poles}}(t) = \frac{\Delta m_N(t) - \Delta m_S(t)}{M\sqrt{7}}. \tag{10}$$

We adopt seasonal mass amplitudes of $|\Delta m_N| = 6.2 \times 10^{15}$ kg and $|\Delta m_S| = 8.4 \times 10^{15}$ kg[28], with $\Delta m_N(t)$ and $\Delta m_S(t)$ varying anti-phase over the Martian year (mass accumulates at one pole as it sublimates from the other). The harmonic components $\Delta C_{\ell 0}^{A,B,p,\,\text{poles}}$ are then obtained by projecting $\Delta C_{\ell 0}^{\text{poles}}(t)$ onto $\cos(\omega t)$ and $\sin(\omega t)$ following Equation 7. The values of $|\Delta m_N|$ and $|\Delta m_S|$ adopted from[28] are empirically calibrated and implicitly absorb the solid-body loading response of the interior to seasonal polar-cap mass exchange. As an additional check of the sensitivity of the inclusion of zonal terms, we perform a tidal tomography inversion which entirely excludes zonal harmonics as constraints. The resulting posterior distributions for this scenario deviate by less than 15% from those of our nominal inversion (see Extended Data Fig. 2).

Tidal Tomography Procedure

To constrain the structure of the Martian interior, we carry out a Bayesian inversion with Markov Chain Monte Carlo (MCMC) and a Metropolis sampling algorithm using PyMC[73]. For our inversion, we vary elastic parameters relative to a reference Martian interior to fit observed $\Delta C_{\ell m}^{A,B}$ and $\Delta S_{\ell m}^{A,B}$ (Table 1). Our detailed procedure is described below.

We consider the impact of 3D perturbations to the shear modulus of a 1D reference model on $\Delta C_{\ell m}^{A,B}$ and $\Delta S_{\ell m}^{A,B}$. Our reference model is fixed (i.e., not sampled) and is based on the analysis of[29] which constrains Martian interior structure using the planet's mean density, moment of inertia, seismic wave arrival times, and the predicted composition of the Martian mantle (see Extended Data Table 2 for assumed mean shear modulus, bulk modulus, and density values for each internal layer). We do not consider lateral changes in density or bulk modulus (the latter of which has a negligible effect on $\Delta C_{\ell m}^{A,B}$ and $\Delta S_{\ell m}^{A,B}$, see[9]) for tidal tomography inversions (COM–COF offset is used only for a-posteriori calculations described in Fig. 3). Since shear modulus (μ) is related to shear wave speed (V_s) and density (ρ) via $\mu = \rho V_s^2$, our approach effectively perturbs V_s while maintaining fixed ρ within each model layer. Note that our choice of reference model could substantially impact the non-coupled response of Mars's interior (i.e., $K_{\ell',m'}^{\ell,m}$ where $\ell, m = \ell', m'$). However, from Equation 5, forcing at $\ell = 3$ harmonics is expected to be negligible (approximately three orders of magnitude smaller) compared to mode coupled responses for these harmonics reported in Table 1, and so are ignored for inversions.

We consider a total of 30 parameters that describe 3D variations in shear modulus (that is, $\ell = 1$–3 for the crust and mantle). These parameters are sampled as coefficients for spherical harmonic basis functions that comprise the ratio of the spatially variable shear modulus μ to that of the fixed reference model μ_{ref} for each internal layer:

$$\frac{\mu}{\mu_{ref}} = \sum_{\ell=1}^{3} \left[\psi_{\ell 0}\, \mu_{\ell 0}\, Y_{\ell 0}(\theta,\lambda) + \sum_{m=1}^{\ell} \left(\psi_{\ell m}^{c}\, \mu_{\ell m}^{c}\, Y_{\ell m}^{c}(\theta,\lambda) + \psi_{\ell m}^{s}\, \mu_{\ell m}^{s}\, Y_{\ell m}^{s}(\theta,\lambda) \right) \right], \quad (11)$$

where the sampled coefficients are $\mu_{\ell 0}$ for $m = 0$ and $(\mu_{\ell m}^{c}, \mu_{\ell m}^{s})$ for $m \geq 1$. By normalizing 3D shear modulus variations by μ_{ref} in Equation 11, we implicitly account for the impact of variations in 1D shear modulus on mode coupled responses such that our choice of reference model does not substantively impact inversion results. As an additional check, we have carried out tidal tomography inversions for which we sample the 1D shear and bulk moduli of the crust and mantle from a Gaussian distribution centered about our nominal reference model values (see Table 2) and with a standard deviation equal to 5% of these values (Extended Data Fig. 2). The resulting posterior distributions for recovered degree-1 variations in mantle shear modulus deviate minimally from those of our nominal inversion.

The real-form spherical-harmonic basis functions (with θ the planetocentric co-latitude in the center-of-mass frame) are:

$$
\begin{aligned}
Y_{\ell 0}(\theta,\lambda) &= \sqrt{\frac{2\ell+1}{4\pi}}\,P_{\ell 0}(\cos\theta),\\
Y^{c}_{\ell m}(\theta,\lambda) &= \begin{cases} \sqrt{\dfrac{(2\ell+1)}{2\pi}\dfrac{(\ell-m)!}{(\ell+m)!}}\,P_{\ell m}(\cos\theta)\cos(m\lambda), & m>0,\\[2ex] 0, & m=0, \end{cases}\\
Y^{s}_{\ell m}(\theta,\lambda) &= \begin{cases} \sqrt{\dfrac{(2\ell+1)}{2\pi}\dfrac{(\ell-m)!}{(\ell+m)!}}\,P_{\ell m}(\cos\theta)\sin(m\lambda), & m>0,\\[2ex] 0, & m=0. \end{cases}
\end{aligned}
\tag{12}
$$

The quantities $\psi_{\ell 0}$, $\psi^{c}_{\ell m}$, and $\psi^{s}_{\ell m}$ indicate coefficients that normalize the right side of Equation 11 so that an input $\mu^{c}_{\ell m}, \mu^{c}_{\ell m}$, or $\mu^{c}_{\ell m}$ of 1 (assuming all other sampled coefficients are zero) corresponds to a peak-to-peak variation in μ/μ_{ref} of -1 to 1 (see, for example,[9] Equation 68). Note that values presented in Fig. 2a–c indicate $\mu_{\ell m}, \mu^{c}_{\ell m}, \mu^{s}_{\ell m} \times 100\%$. To generate prior distributions, we parameterize $\mu_{\ell m}, \mu^{c}_{\ell m}, \mu^{s}_{\ell m}$ in Equation 11 in terms of their base-10 logarithm (that is, $\mu'_{\ell m}, {\mu^{c}}'_{\ell m}, {\mu^{s}}'_{\ell m}$):

$$
\begin{aligned}
\mu'_{\ell m} &= \log_{10}(1+\mu_{\ell m})\,,\\
{\mu^{c}}'_{\ell m} &= \log_{10}(1+{\mu^{c}}_{\ell m})\,,\\
{\mu^{s}}'_{\ell m} &= \log_{10}(1+{\mu^{s}}_{\ell m})\,.
\end{aligned}
\tag{13}
$$

To generate ensembles of internal structure models for Markov chains, we sample uniform (that is, flat) prior probability distributions for $\mu'_{\ell m}, {\mu^{c}}'_{\ell m}, {\mu^{s}}'_{\ell m}$ (that correspond to a range of $\mu_{\ell m}, \mu^{c}_{\ell m}, \mu^{s}_{\ell m} \times 100\%$ from -200% to 200%) and forward compute

$\Delta C_{\ell m}^{A,B,p}$ and $\Delta S_{\ell m}^{A,B,p}$ using these values. Each ensemble consists of ~10000 individual accepted model realizations (i.e., approximately 500,000 samples total from 50 walkers). To speed up convergence, we adopt an adaptive sampling approach (the 'tune' functionality in PyMC) which dynamically adjusts step sizes based on the sensitivity of model outputs to input parameters[73]. We visually inspect Markov chains to discard initial burn-in steps (i.e., typically the first ~10−20% of samples) and terminate inversions when parameter autocorrelation values are > 0.99. Walker positions are updated based on the likelihood function L:

$$\log L \propto -\frac{1}{2}(\mathbf{X}-\mathbf{Y})^T \mathbf{\Sigma}^{-1}(\mathbf{X}-\mathbf{Y}), \tag{14}$$

where $\mathbf{X}$ is the vector of observed $\Delta C_{\ell m}^{A,B}$ and $\Delta S_{\ell m}^{A,B}$ in Equation 2 (that is, parameters in Table 1 and Extended Data Table 1) and $\mathbf{Y}$ is the vector of model-predicted $\Delta C_{\ell m}^{A,B,p}$ and $\Delta S_{\ell m}^{A,B,p}$ in Equation 7. For a comparison of model-predicted posteriors of $\Delta C_{\ell m}^{A,B,p}$ and $\Delta S_{\ell m}^{A,B,p}$ to observations, see Extended Data Fig. 3. $\mathbf{\Sigma}$ is a diagonal matrix (i.e., each entry is independent) that incorporates observational covariances (i.e., 15× formal uncertainties presented in Table 1). Other potential system constraints (for example, mean density, moment of inertia, or quality factors) are not incorporated into vectors $\mathbf{X}$ or $\mathbf{Y}$ in Equation 14.

Modeling Temperature and Iron Content

In this section, we outline our methodology for the calculations shown in Figure 3 of the main text. We parameterize hemispheric variations in effective shear modulus in terms of the combined effect of temperature and composition on rheology:

$$\Delta\mu = \Delta T \frac{d\mu}{dT} + \Delta X_{\mathrm{Fe}} \frac{d\mu}{dX_{\mathrm{Fe}}}, \tag{15}$$

where ΔT is the hemispheric temperature contrast and ΔX_{Fe} is the hemispheric contrast in fayalite–forsterite mol fraction (Fa–Fo). To compute $\frac{d\mu}{dT}$, we fit shear modulus versus forcing timescale data from Fig. 1a[35] (the "background-only" Burgers model, note that all other calculations for tidal tomography inversions assume a purely elastic rheology) with power-law functions and extend these curves to the Martian annual forcing period (5.94×10^7 s; see Extended Data Fig. 6) yielding:

$$\frac{d\mu}{dT} \approx -0.204 \text{ GPa K}^{-1}, \tag{16}$$

We note that several anelastic laws have been published (e.g.,[74;75]), but we have chosen that of[35] as it has been used in several analogous applications for the Moon[76], Mars[77], and the Earth[78;79]. While each anelastic law differs in details, the overall trend of shear modulus softening with lower frequency across all experimental laws is consistent. For compositional variations, we adopt $\frac{d\mu}{dX_{\text{Fe}}} = -0.3$ GPa per % Fa–Fo based on experimental data presented in[80].

We evaluate the impact of degree-1 variations in density on Mars's COM–COF offset (that is, $\delta z_{COM-COF}$) by first assuming an offset vector of the form:

$$\delta z_{COM-COF} = \frac{1}{M} \int_V z\rho(\mathbf{r})\, dV, \tag{17}$$

where $\mathbf{r}$ is the position vector within Mars, $\rho(\mathbf{r})$ is the local density, z is the component of $\mathbf{r}$ along the asymmetry axis, V is the volume of the planet, and M is its mass. Converting Equation 17 into spherical harmonics and integrating over the radial extent of the mantle, we obtain:

$$\delta z_{COM-COF} = \frac{1}{M} \sqrt{\frac{\pi}{12}}\, \Delta\rho \left(r^4_{Moho} - r^4_{CMB} \right), \tag{18}$$

where $M = 6.4171 \times 10^{23}$ kg is the mass of Mars, r_{Moho} and r_{CMB} are respectively the radii of Mars's Moho and core–mantle boundary, and $\Delta\rho$ is the peak-to-peak amplitude of degree-1 variations in mantle density. We compute $\Delta\rho$ by assuming linear contributions from thermal expansion and iron enrichment:

$$\Delta\rho = -\rho_{\mathrm{ref}}\beta\Delta T + \Delta X_{\mathrm{Fe}}\frac{d\rho}{dX_{\mathrm{Fe}}}, \tag{19}$$

where $\rho_{\mathrm{ref}} = 3500$ kg m^{-3} is a representative mantle density, $\beta = 3 \times 10^{-5}$ K^{-1} is the volume thermal expansion coefficient, and $\frac{d\rho}{dX_{\mathrm{Fe}}} = 9.7$ kg m^{-3} per % Fa–Fo is the assumed density sensitivity to iron enrichment, following[4]. Equation 19 is formulated in terms of lateral density perturbations relative to a reference mantle, so the absolute mantle density and baseline iron content do not directly affect the calculation except insofar as they modify the adopted transfer function $\frac{d\rho}{dX_{\mathrm{Fe}}}$.

For comparison with these calculations, we adopt COM–COF offsets from Table 4 of[36], which gives $\Delta x = 233$ m, $\Delta y = 1428$ m, and $\Delta z = 2986$ m, corresponding to a total offset magnitude of 3.3 km. Although[36] do not report a formal uncertainty for this quantity, uncertainties are expected to be small (< 0.02 km) relative to the 0–1.31 km range used here. We project the vector of the COM-COF offset onto the axis defined by the maximum shear modulus asymmetry in Figure 2d (45°N, 138°W), which yields an upper-bound contribution of density variations in the mantle to COM–COF offset of 1.31 km. The lower bound of 0 km used in Figure 3 corresponds to the opposite end-member case in which the observed COM–COF offset is explained entirely by crustal structure (for example, a case in which surface topography produces a COF shift of 1.31 km).

We note that the 0–1.31 km range is an approximate (that is, order-of-magnitude) estimate of the impact of mantle density on COM–COF offset and therefore does not encompass the full range of possible degree-1 density variations in the interior. For example, Moho relief can change the COM–COF offset by >50% if this effect is not negated by the impact of surface topography on the COM (e.g., via Airy isostasy). Similarly, the depth dependence of $\frac{d\rho}{dX_{\mathrm{Fe}}}$, including the impact of a possible density crossover near 600–700 km depth, could change the COM–COF offset by up to few hundred meters. Even so, these effects (and the 0–1.31 km range) are much smaller than the several tens of kilometers in COM–COF offset that would be required to explain the asymmetries shown in Figure 3 purely in terms of compositional variations (e.g., iron enrichment) in the mantle.

Martian Melt Ascent

Here we estimate the approximate timescale of ascent for melt for Mars's mantle.[44] gives the characteristic timescale Λ for a small melt fraction to separate from a partially–molten layer of thickness h:

$$\Lambda = \frac{h\eta\psi}{\kappa\,\Delta\rho\,g} \tag{20}$$

η is the melt viscosity, ψ is the melt fraction, $\Delta\rho$ is the density contrast between melt and matrix, g is the acceleration due to gravity and κ is the permeability. For small melt fractions the permeability is taken to be:

$$\kappa = \frac{d^2\,\psi^n}{C} \tag{21}$$

Here d is the grain size, $n = 2$ and $C = 3000$. For the Martian mantle, we will take $h = 300$ km, $\Delta\rho = 100$ $\mathrm{kg\,m^{-3}}$, $g = 3.7$ $\mathrm{m\,s^{-2}}$ and a grain size of 1 mm. If the areotherm crosses the solidus at 300 km depth, the temperature of the melts will be in the range 1700–1800 K. The resulting viscosity of Martian basaltic melts at these temperatures is roughly 1 Pa s[81]. For a melt fraction of 0.02, the permeability is then $\sim 10^{-13}$ m^2 and the compaction timescale is ~ 3 Myr.

Methods References

[56] Pavlis, D. E. & Nicholas, J. B. GEODYN II system description (vols. 1–5). contractor report, SGT Inc., Greenbelt, MD (2017). URL https://earth.gsfc.nasa.gov/geo/data/geodyn-documentation.

[57] Konopliv, A. S., Park, R. S. & Folkner, W. M. An improved JPL Mars gravity field and orientation from Mars orbiter and lander tracking data. *Icarus* **274**, 253–260 (2016).

[58] Millour, E. *et al.* The mars climate database (version 5.3). Tech. Rep. URL http://www-mars.lmd.jussieu.fr.

[59] Wagner, N. L., James, P. B., Ermakov, A. I. & Sori, M. M. Evaluating the use of seasonal surface displacements and time-variable gravity to constrain the interior of mars. *Journal of Geophysical Research: Planets* **129** (2024).

[60] Berne, A., Simons, M., Keane, J. & Park, R. S. Inferring the mean thickness of the outer ice shell of enceladus from diurnal crustal deformation. *Journal of Geophysical Research: Planets* **128**, e2022JE007712 (2023).

[61] Berne, A., Simons, M., Keane, J. & Park, R. S. Using tidally-driven elastic strains to infer regional variations in crustal thickness at enceladus. *Geophysical Research Letters* **50**, 311–318 (2023).

[62] Spitale, J. N. *et al.* Curtain-based maps of eruptive activity in enceladus's south-polar terrain at 15 cassini epochs. *The Planetary Science Journal* **6**, 67 (2025). URL https://doi.org/10.3847/PSJ/adb7d7.

[63] Bagheri, A. *et al.* Exploring the interior structure and mode of tidal heating in enceladus. *The Planetary Science Journal* **6**, 245 (2025). URL https://iopscience.iop.org/article/10.3847/PSJ/ae0cab/meta.

[64] Berne, A. C. *Tidal Dynamics of Laterally Heterogeneous Planetary Bodies*. Ph.D. thesis, California Institute of Technology (2026). URL https://resolver.caltech.edu/CaltechTHESIS:08022025-042237605.

[65] Park, R. S. *et al.* The global shape, gravity field, and libration of enceladus. *Journal of Geophysical Research: Planets* **129**, e2023JE008054 (2024).

[66] Meyer, C. R. *et al.* Implications of shallow–shell models for topographic relaxation on icy satellites. *Journal of Geophysical Research: Planets* **130**, e2025JE009247 (2025).

[67] Bruinsma, S. & Lemoine, F. G. A preliminary semiempirical thermosphere model of mars: Dtm-mars. *Journal of Geophysical Research: Planets* **107**, 5085 (2002).

[68] Sanchez, B. V., Rowlands, D. D. & Haberle, R. M. Variations of mars' gravitational field based on the nasa/ames general circulation model. *Journal of Geophysical Research: Planets* **111**, E06010 (2006). URL https://doi.org/10.1029/2005JE002442.

[69] Madeleine, J.-B., Forget, F., Millour, E., Montabone, L. & Wolff, M. J. Revisiting the radiative impact of dust on Mars using the LMD Global Climate Model. *Journal of Geophysical Research: Planets* **116**, E11010 (2011).

[70] Genova, A. *et al.* Long-term variability of co2 and o in the mars upper atmosphere from mro radio science data. *Journal of Geophysical Research: Planets* **120**, 849–868 (2015).

[71] Rovira-Navarro, M. *et al.* Prospects of using tidal tomography to constrain ganymede's interior. *Geophysical Research Letters* **52**, e2025GL114708 (2025). URL https://doi.org/10.1029/2025GL114708.

[72] Rovira-Navarro, M. *et al.* *Using tidal tomography to unveil the 3d structure of moons*. In *EPSC-DPS Joint Meeting 2025*, EPSC-DPS2025-49 (Copernicus Meetings, 2025).

[73] Patil, A., Huard, D. & Fonnesbeck, C. J. Pymc: Bayesian stochastic modelling in python. *Journal of Statistical Software* **35** (2010).

[74] Yamauchi, H. & Takei, Y. Polycrystal anelasticity at near-solidus temperatures. *Journal of Geophysical Research: Solid Earth* **121**, 7790–7820 (2016).

[75] McCarthy, C., Takei, Y. & Hiraga, T. Experimental study of attenuation and dispersion over a broad frequency range: 2. the universal scaling of polycrystalline materials. *Journal of Geophysical Research: Solid Earth* **116**, B09207 (2011).

[76] Nimmo, F., Faul, U. H. & Garnero, E. J. Dissipation at tidal and seismic frequencies in a melt-free Moon. *Journal of Geophysical Research: Planets* **117**, E09005 (2012).

[77] Nimmo, F. & Faul, U. H. Dissipation at tidal and seismic frequencies in a melt-free, anhydrous Mars. *Journal of Geophysical Research: Planets* **118**, 2558–2569 (2013).

[78] Dalton, C. A. & Faul, U. H. The oceanic and cratonic upper mantle: Clues from joint interpretation of global velocity and attenuation models. *Lithos* **120**, 160–172 (2010).

[79] Lau, H. C. P. & Faul, U. H. Anelasticity from seismic to tidal timescales: Theory and observations. *Earth and Planetary Science Letters* **508**, 18–29 (2019).

[80] Chung, D. H. Effects of iron/magnesium ratio on P-wave and S-wave velocities in olivine. *Journal of Geophysical Research* **75**, 7353–7361 (1970). URL https://doi.org/10.1029/JB075i035p07353.

[81] Chevrel, M. O., Baratoux, D., Hess, K. U. & Dingwell, D. B. Viscous flow behavior of tholeiitic and alkaline Fe-rich martian basalts. *Geochimica et Cosmochimica Acta* **124**, 348–365 (2014).

Data Availability. The MGS, ODY, and MRO data used to generate the results of this paper are available at the NASA Planetary Data System Geosciences Node (http://pds-geosciences.wustl.edu/missions/mgs/rsraw.html, http://pds-geosciences.wustl.edu/missions/odyssey/radioscience.html, http://pds-geosciences.wustl.edu/mro/mro-m-rss-1-magr-v1/mrors_0xxx/).

Code Availability. The gravity recovery results presented in this study were generated using the GEODYN II orbit determination and geodetic parameter estimation software[56]. The publicly distributed NASA build of GEODYN can be obtained via https://space-geodesy.nasa.gov/techniques/tools/GEODYN/GEODYN.html. The software LOV3D is also available at GitHub (https://github.com/mroviranavarro/LOV3D_multi), and an example script to evaluate gravity coefficients for a trial Martian interior model corresponding to the maximum a-posteriori solution from our inversion (and estimates of forcing potential amplitudes based on Eq. 5 and planetary ephemerides over the MGS, ODY, and MRO mission durations) is availabile on Zenodo (https://zenodo.org/records/20823473; https://doi.org/10.5281/zenodo.20823473).

Acknowledgments. We thank two anonymous reviewers for their contribution to the peer review of this work. We thank the Keck Institute for Space Studies (KISS) at the California Institute of Technology for organizing workshops about "Next-Generation Planetary Geodesy" and "Digital Twins for Solar System Exploration" which provided insight, expertise, and discussions that inspired this research.

Funding Statement. This research was supported by a NASA ROSES Solar System Workings (SSW) grant (no. 80NSSC23K1276) (Al.B., I.M.). N.L.W. was supported by the LunaSCOPE NASA SSERVI node (grant 80NSSC23M0161). S.G. was supported by NASA's Planetary Science Division Research Program through the ISFM work package Planetary Geodesy at the Goddard Space Flight center. A.G. acknowledges funding from ASI grant no. 2023-60- HH.0.

Contributions

Al.B. conceived and designed this study under the supervision of I.M.. Al.B. drafted the article and constructed Figures 1-4. N.W. provided expertise regarding modeling Mars's atmosphere to produce coefficients presented in Table 1. Al.B., S.G. and

A.G. analyzed the spacecraft data to determine a model of Mars's static and time-varying gravity field. M.R.N., Am.B., and C.Q. developed numerical models used for predicting tidal deformation for laterally heterogeneous bodies in the study. K.C. and S.Z. provided expertise regarding the extent that formation scenarios for the crustal dichotomy can be constrained from results presented in this study. Am.B., F.N., A.M., and H.L. provided insight into the relationship between partial melt and the dissipative properties of Mars's mantle. D.H. provided expertise regarding the relationship between partial melt and magnetism in this study. F.N. provided expertise regarding the relationship between tectonics, volcanism, and the presence of mantle partial melt for Mars. All authors discussed the results of the study and commented on the manuscript at each stage of revision.

Competing Interests

The authors declare no competing interests.

Ethics

This study did not involve human participants, human data or tissue, or animals, and therefore no ethical approval or informed consent was required. The work is based entirely on the analysis of publicly available spacecraft tracking and gravity data, and complies with all relevant institutional, national, and international guidelines and regulations.

Extended Data Legends

Extended Data Table 1 Recovered degree-2 and zonal degree-3 time-varying gravity field for Mars with 15x formal uncertainties. Coefficient amplitudes are 4π-normalized and evaluated over the seasonal, 687-day period referenced to the J2000 epoch. Superscripts A and B denote in-phase (cosine) and out-of-phase (sine) signal components.

Extended Data Table 2 Assumed 1D reference interior model for Mars. Columns indicate the radial range, density, bulk modulus, and shear modulus of each layer. Model is constrained by Mars's degree-2 tidal deformation, Moment of Inertia, Mean density, and seismic wave arrival times [29]

Extended Data Table 3 Inverted shear modulus coefficients for Mars's interior. Columns indicate the 50th, 0.3rd, and 99.7th percentile ranges of posterior distributions for coefficients in the Crust (left column set) and Mantle (right column set).

Extended Data Fig. 1 Seasonal evolution and atmospheric-model sensitivity of the degree-3 gravity signals. (a) Seasonal evolution of degree-3 gravity coefficients across models for Mars's atmosphere. Curves show the 4π-normalized, demeaned seasonal time series of ΔC_{30}, ΔC_{31}, ΔS_{31}, ΔC_{32}, ΔS_{32}, ΔC_{33}, and ΔS_{33} as a function of solar longitude L_s. Colored curves denote the average-extreme ultraviolet (EUV) (red), warm/max-EUV with dust (pink), and cold/min-EUV with dust (orange) atmospheric scenarios, while gray curves show the individual realizations of the Avg EUV model from MY24 through MY35. Error bars in Fig.1a of the main text are derived from inter-annual variations for the Avg EUV model. Horizontal gray lines mark zero amplitude in each panel. **(b)** Sensitivity of the degree-3 gravity signals to atmospheric models and assumed loading Love numbers. Bars show the total observed seasonal degree-3 perturbations (green), the nominal atmospheric correction using the average-EUV scenario (red), atmospheric corrections for the cold/minimum-EUV/dust and warm/maximum-EUV/dust endmember scenarios (orange and pink), and cases with 0% and 200% the loading Love numbers k'_ℓ assigned to the nominal Average EUV atmosphere (purple and brown, see Equation 3 of the main text). The left and right groups show the cosine and sine terms, respectively. Error bars on the observations denote 15× formal uncertainties.

Extended Data Fig. 2 Sensitivity of tidal tomography results to atmospheric models, assumed loading Love numbers, the choice of reference 1D interior model, and the inclusion of zonal gravity field terms. Posterior distributions of the degree-1 mantle shear-modulus coefficients for **(a)** the meridional $\ell = 1$, $m = 1$ term, **(b)** the north–south $\ell = 1$, $m = 0$ term, and **(c)** the east–west $\ell = 1$, $m = -1$ term for scenarios of the nominal atmospheric correction using the average-EUV scenario (red), atmospheric corrections for the cold/minimum-EUV/dust and warm/maximum-EUV/dust endmember scenarios (orange and pink), cases with 0% and 200% the loading Love numbers k'_ℓ assigned to the nominal Average EUV atmosphere (purple and brown, see Equation 3 of the main text), a case where the reference shear and bulk moduli of the crust and mantle are sampled from a Gaussian distribution centered about nominal values (see Extended Data Table 2) and a standard deviation equal to 5% of these values (light blue), and an inversion that excludes the zonal gravity harmonics in Extended Data Table 1 as constraints (green). Median shifts for each scenario relative to the average EUV case is shown to the left in each plot.

Extended Data Fig. 3 Posterior distributions of annual gravity coefficient variations. Panels show normalized histograms for the posteriors of **(a)** degree-2 and **(b)** degree-3 annual variations in gravity coefficients ($\Delta C_{\ell m}^{A,B}$ and $\Delta S_{\ell m}^{A,B}$) obtained from tidal tomography inversions. Gray shaded regions denote 45× the formal uncertainty derived from gravity field inversions (that is, 3× the 15× 1-σ uncertainties in Table 1 and Extended Data Table 1).

Extended Data Fig. 4 Posterior distributions of perturbations in the shear modulus of Mars's crust and mantle. **(a)** Mars's crust and **(b)** Mars's mantle. In each panel, top row: degree-1 ($\ell = 1$, $m = 1, 0, -1$); middle row: degree-2 ($\ell = 2$, $m = -2, -1, 0, 1, 2$); bottom row: degree-3 ($\ell = 3$, $m = -3, -2, -1, 0, 1, 2, 3$). Vertical lines mark $x = 0$ (dotted), the 0.3% and 99.7% percentiles (solid gray), and the 50th percentile (solid red).

Extended Data Fig. 5 Corner plots for degree-1 shear-modulus perturbations in an inversion with the mantle subdivided into multiple layers. Degree-1 coefficients **(a)** μ_{11}^{C}, **(b)** μ_{10}, and **(c)** μ_{11}^{S} are derived for an inversion that subdivides the martian mantle into a lower portion (radius 1830 - 2520 km) and an upper portion (radius 2520 - 3340 km). Pearson correlation coefficients R are shown alongside 2D posterior distributions (values close to -1 indicate a substantially non-unique trade-off between recovered heterogeneity amplitudes). Red lines on 1D histograms indicate the median (50^{th} percentile) of distributions. Gray vertical lines in 1D histograms indicate values expected for a laterally isotropic reference interior.

Extended Data Fig. 6 Sensitivity of olivine shear modulus to temperature at the Martian annual period. (a) Shear modulus versus oscillation period for the background-only Burgers model of olivine rheology evaluated from experiments on crystals at temperatures between 700–1200°C (see Fig. 1a of[35]). Colored curves are power-law fits extended beyond the range of experimental data (gray shading) to the Martian annual period (5.94×10^7 s; dashed vertical line). **(b)** Shear moduli evaluated at the Martian annual period as a function of temperature. A linear trendline (red) yields $d\mu/dT \approx -0.204$ GPa K^{-1} which is used to recover hemispheric variations in temperature from shear modulus asymmetries (see Fig. 3).

Extended Data Fig. 7 Post-fit residuals and empirical acceleration amplitude change with inclusion of $\ell = 3$ time-variable gravity. Comparison of gravity field inversion solutions without (blue) and with (red) inclusion of degree-3 time-varying gravity terms; the green dashed line (right axis) shows the difference between solutions. Arcs are drawn from 2017 data are not used in the gravity field determination. **(a)** RMS of fit (Hz). **(b)** Along-track empirical acceleration amplitude. **(c)** Cross-track empirical acceleration amplitude.